



# Results of the Interlaboratory Computational Fluid Dynamics Study of the FDA Benchmark Blood Pump

SAILAHARI V. PONNALURI,<sup>1,2</sup> PRASANNA HARIHARAN,<sup>1</sup> LUKE H. HERBERTSON,<sup>1</sup>  
KEEFE B. MANNING,<sup>2,3</sup> RICHARD A. MALINAUSKAS,<sup>1</sup> and BRENT A. CRAVEN<sup>1</sup> 

<sup>1</sup>Division of Applied Mechanics, Office of Science and Engineering Laboratories, Center for Devices and Radiological Health, U.S. Food and Drug Administration, Silver Spring, MD, USA; <sup>2</sup>Department of Biomedical Engineering, The Pennsylvania State University, University Park, PA, USA; and <sup>3</sup>Department of Surgery, Penn State Hershey Medical Center, Hershey, PA, USA

(Received 27 June 2022; accepted 21 October 2022; published online 18 November 2022)

Associate Editor Joel Stitzel oversaw the review of this article.

**Abstract**—Computational fluid dynamics (CFD) is widely used to simulate blood-contacting medical devices. To be relied upon to inform high-risk decision making, however, model credibility should be demonstrated through validation. To provide robust data sets for validation, researchers at the FDA and collaborators developed two benchmark medical device flow models: a nozzle and a centrifugal blood pump. Experimental measurements of the flow fields and hemolysis were acquired using each model. Concurrently, separate open interlaboratory CFD studies were performed in which participants from around the world, who were blinded to the measurements, submitted CFD predictions of each benchmark model. In this study, we report the results of the interlaboratory CFD study of the FDA benchmark blood pump. We analyze the results of 24 CFD submissions using a wide range of different flow solvers, methods, and modeling parameters. To assess the accuracy of the CFD predictions, we compare the results with experimental measurements of three quantities of interest (pressure head, velocity field, and hemolysis) at different pump operating conditions. We also investigate the influence of different CFD methods and modeling choices used by the participants. Our analyses reveal that, while a number of CFD submissions accurately predicted the pump performance for individual cases, no single participant was able to accurately predict all quantities of interest across all conditions. Several participants accurately predicted the pressure head at all conditions and the velocity field in all but one or two cases. Only one of the eight participants who submitted hemolysis results accurately predicted absolute plasma free hemoglobin levels at a majority of the conditions, though most participants were successful at predicting relative hemolysis levels between

conditions. Overall, this study highlights the need to validate CFD modeling of rotary blood pumps across the entire range of operating conditions and for all quantities of interest, as some operating conditions and regions (e.g., the pump diffuser) are more challenging to accurately predict than others. All quantities of interest should be validated because, as shown here, it is possible to accurately predict hemolysis despite having relatively inaccurate predictions of the flow field.

**Keywords**—CFD, Blood pump, Validation, Particle image velocimetry.

## INTRODUCTION

Computational fluid dynamics (CFD) modeling is widely used to simulate blood-contacting medical devices such as stents,<sup>6,15,29</sup> inferior vena cava filters,<sup>2–4,35</sup> artificial heart valves,<sup>5,20,21</sup> and mechanical circulatory support devices.<sup>13,14,24,32</sup> Simulations can be used throughout the medical device total product life cycle,<sup>25</sup> from design ideation to postmarket analysis. Historically, CFD has been most commonly used for device design and optimization, and more recently it has been used as a complement to inform laboratory experiments conducted to demonstrate device safety or effectiveness in regulatory submissions to the U.S. Food and Drug Administration (FDA). As computational methods and technologies continue to mature, more influential uses of CFD are on the horizon. To be relied upon to inform high-risk decision making, however, the CFD predictions should be shown to be credible to a degree that is commensurate with the risk

Address correspondence to Brent A. Craven, Division of Applied Mechanics, Office of Science and Engineering Laboratories, Center for Devices and Radiological Health, U.S. Food and Drug Administration, Silver Spring, MD, USA. Electronic mail: brent.craven@fda.hhs.gov

associated with the decision.<sup>1,36</sup> Generally, model credibility is established by performing verification, validation, and uncertainty quantification (VUQ).<sup>1,19,28,31</sup>

To provide robust data sets for CFD validation, researchers at the FDA and collaborators developed two benchmark medical device flow models: a nozzle and a centrifugal blood pump.<sup>22</sup> Experimental pressure, velocity, and hemolysis data were acquired for each model in up to three independent laboratories.<sup>16–18,22</sup> To assess the state of the technology for CFD modeling of medical devices, the FDA also initiated separate open interlaboratory CFD studies in which participants from around the world submitted simulation predictions of each benchmark model. Importantly, in each case the participants were blinded to the experimental data so as not to bias or influence the predictions. The results of the first interlaboratory CFD study of the FDA nozzle were reported by Stewart *et al.*<sup>33,34</sup>

The main objective of this study is to report the results of the second FDA interlaboratory CFD study of the benchmark centrifugal blood pump. A total of 24 CFD submissions were received using different flow solvers, mesh topologies and resolutions, time integration schemes, and turbulence models. Here, we report the complete results of the interlaboratory study that include comparisons of the CFD predictions with experimental pressure, velocity field, and hemolysis measurements at several different pump operating conditions. As part of the analysis, we also investigate the predictive accuracy of the CFD results as a function of the different meshing and simulation parameters used by the participants. Details of the FDA-led interlaboratory experimental and computational studies are publicly available online, along with a bibliography of publications that are based on these data ([https://ncihub.org/wiki/FDA\\_CFD](https://ncihub.org/wiki/FDA_CFD)).

## MATERIALS AND METHODS

### *FDA Benchmark Blood Pump and Flow Loop*

The benchmark centrifugal blood pump (Fig. 1a) was designed to have a relatively simple geometry and operate over a wide range of flow, pressure, and pump speed conditions. The dimensions of the pump geometry and three-dimensional computer aided design (CAD) files are publicly available at [https://ncihub.org/wiki/FDA\\_CFD/ComputationalRoundRobin2](https://ncihub.org/wiki/FDA_CFD/ComputationalRoundRobin2) Pump. Briefly, the main components of the pump include the rotor, housing, and outlet diffuser. The pump rotor is 52 mm in diameter and includes four simplified blades that are equally spaced in the circumferential

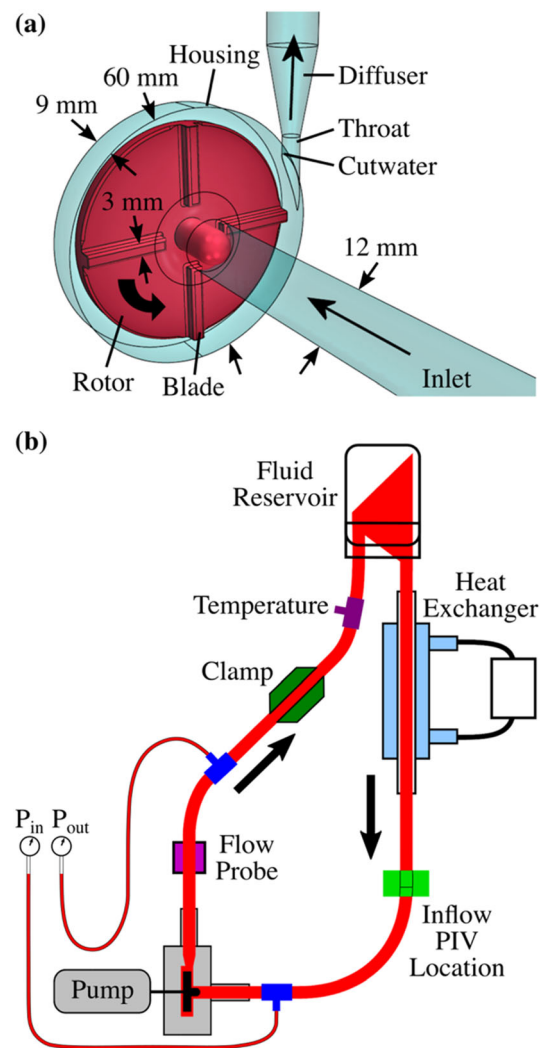


**FIGURE 1.** Schematic illustration of (a) the FDA benchmark blood pump and (b) the experimental flow loop. Adapted from Hariharan *et al.*<sup>16</sup>

direction about the rotor hub. Each rotor blade is 3 mm wide, 3 mm in height, and 18.5 mm long. All of the edges between blade surfaces are filleted with measured radii between 0.17 and 0.60 mm. The pump housing has an inner diameter of 60 mm and an inner height of 9 mm. The rotor is centered in the pump housing with gap clearances of: 4 mm in the radial gap between the outer edge of the rotor and the housing, 1 mm between the top of the rotor blades and the housing, and 1 mm between the back of the rotor disk and the housing. After being propelled by the rotor, fluid exits the pump through a narrow throat that transitions to an outlet diffuser (Fig. 1a). The abrupt geometric transition from the housing to the throat is known as the “cutwater,” which in the FDA pump was filleted with a minimum measured radius of 40  $\mu$ m. Three identical blood pump models were fabricated from acrylic to enable optical access for particle image

velocimetry (PIV), which was performed concurrently in three independent laboratories.

The pump was placed in a well-characterized experimental flow loop to make measurements of the pressure head, velocity field, and hemolysis (Fig. 1b). The details of the experimental setups are described by Hariharan et al.<sup>16</sup> and Malinauskas et al.<sup>22</sup> To summarize, the pump inlet was connected to a curved, 12 mm diameter tube with a constant radius of curvature upstream of the inlet of 9 cm. A flow-through heat exchanger maintained the temperature of the working fluid, which was monitored with an inline thermistor. A pressure transducer was connected to the inlet tube to measure the pump inlet pressure. An ultrasonic flow probe and a second pressure transducer were used to measure the flow rate and pressure in the outlet tube, respectively, upstream of an adjustable clamp that was used to control the back-pressure on the pump and the flow rate during the experiments. As illustrated in Fig. 1b, the pump pressure differential (or pressure head) was quantified as the difference in the pressure between the outlet and inlet transducers, measured at the same height after zeroing the transducers prior to each experiment to compensate for the hydrostatic component. This was done to enable a direct comparison with pressure predictions from CFD without having to account for the hydrostatic pressure between the inlet and outlet measurement locations in the flow loop.

#### Fluid Properties and Operating Conditions

PIV and hemolysis experiments were performed with the benchmark blood pump at six different operating conditions defined in terms of the two independent non-dimensional parameters that characterize pump performance, namely the pump Reynolds number (Re) and the volumetric flow coefficient ( $\Phi$ ), defined respectively as:<sup>9</sup>

$$\text{Re} = \frac{\rho \Omega D^2}{\mu} \quad (1)$$

$$\Phi = \frac{Q}{\Omega D^3} \quad (2)$$

where  $\rho$  is the fluid density,  $\mu$  is the fluid dynamic viscosity,  $\Omega$  is the pump angular rotational speed,  $D$  is the rotor diameter, and  $Q$  is the volumetric flow rate. The six pump operating conditions are summarized in Table 1.

As described by Hariharan et al.,<sup>16</sup> interlaboratory PIV experiments were conducted in three independent labs using a Newtonian blood analog fluid comprised of sodium iodide, water, and glycerin. Sodium iodide was used to match the index of refraction of the acrylic blood pump to facilitate distortion-free optical transparency for PIV. Prior to starting the PIV experiments each day, the fluid density and viscosity were measured. The pump speed ( $\Omega$ ) and the flow rate ( $Q$ ) were then set and fine-tuned to obtain the desired pump Reynolds number and flow coefficient for each of the six operating conditions (Table 1). For consistency with the hemolysis experiments, the PIV measurements were dimensionalized using nominal Newtonian blood properties of  $\rho = 1035 \text{ kg/m}^3$  and  $\mu = 3.5 \text{ cP}$ . Table 1 also lists the corresponding pump speed and flow rate for each operating condition, which were calculated using the nominal blood properties. As summarized, the pump speed ranged from 2500 to 3500 rpm and the flow rate ranged from 2.5 to 7.0 L/min.

As described by Malinauskas et al.,<sup>22</sup> the hemolytic potential of the FDA benchmark blood pump was quantified through *in vitro* tests at one lab. The six pump operating conditions were tested in a randomized fashion using two identical benchmark pumps and a comparative clinical control pump. For each experiment, the flow loop was filled with 250 mL of anticoagulated porcine blood with the hematocrit ( $H_{ct}$ ) adjusted to  $36 \pm 1\%$  and a measured total blood hemoglobin concentration (Hb) of  $11.1 \pm 0.4 \text{ g/dL}$ . The blood was anticoagulated during collection with acid citrate dextrose solution A (ACDA) at a ratio of 15 parts ACDA:85 parts blood. The blood density and the dynamic viscosity at a shear rate of  $500 \text{ s}^{-1}$  were

TABLE 1. Operating conditions for experimental testing of the FDA benchmark centrifugal blood pump.

Condition #	Flow rate (L/min)	Pump speed (rpm)	Reynolds number (Re)	Flow coefficient ( $\Phi$ )
1	2.5	2500	209,338	0.00113
2	2.5	3500	293,073	0.00081
3	4.5	3500	293,073	0.00146
4	6.0	2500	209,338	0.00272
5	6.0	3500	293,073	0.00194
6	7.0	3500	293,073	0.00226

Flow rate and pump rotational speed calculated for each operating condition (defined by Re and  $\Phi$ ) from Eqs. (1) and (2) using nominal blood properties of  $\rho = 1035 \text{ kg/m}^3$  and  $\mu = 3.5 \text{ cP}$ .

measured to be  $1030 \pm 10 \text{ kg/m}^3$  and  $3.4 \pm 0.5 \text{ cP}$ , respectively, which correspond to the nominal blood properties used to scale the PIV data. Measurements of plasma free hemoglobin concentration (fHb) were acquired from blood samples drawn every 40 min during each two-hour experiment. At least 15 replicate hemolysis tests were performed with the benchmark blood pumps relative to eight replicate experiments with the clinical control pump.

### Experimental Data

Both the PIV and hemolysis experiments were performed at all six pump operating conditions to provide a benchmark data set for CFD validation. Inlet and outlet pressures were also measured during both PIV and hemolysis testing. All data are publicly available at [https://nciphub.org/wiki/FDA\\_CFD/ComputationalRoundRobin2Pump](https://nciphub.org/wiki/FDA_CFD/ComputationalRoundRobin2Pump).

For PIV, a total of four data sets were acquired among the three labs, with one lab acquiring two separate sets of measurements to quantify intra-laboratory variability in the data.<sup>16</sup> Planar PIV measurements were acquired in a number of different regions throughout the pump with Hariharan *et al.*<sup>16</sup> reporting data in five key regions that include: (i) the inflow tube (see Fig. 1b), (ii) quadrant 1 in a blade passage plane located 1.2 mm below the top surface of the rotor blades, (iii) quadrant 2 in the same blade passage plane, (iv) the outlet diffuser in the same blade passage plane (see Fig. 2), and (v) a plane in the back-gap region located 0.5 mm from the back of the rotor disk. A total of 500–2500 PIV image pairs, depending on the lab, were phase-averaged with a blade oriented perpendicular to the outlet, as illustrated in Fig. 2. The spatial resolution of the PIV data ranged from 0.25 to 0.55 mm, depending on the lab and the specific measurement region. The planar phase-averaged velocity and the root mean square (RMS) velocity fields were reported in each region by Hariharan *et al.*<sup>16</sup>

Measurements of the plasma free hemoglobin concentration (fHb) for the benchmark blood pump were significantly higher than those measured for the comparator clinical control pump. The measured values of fHb were also linear with time and generally less than 1% of the total hemoglobin concentration, indicating that the levels of hemolysis were small enough such that there was no change in the blood hematocrit during the experiments. Malinauskas *et al.*<sup>22</sup> report the mean and standard deviation (SD) of the fHb values measured at each pump operating condition. In addition to absolute levels of fHb, the original interlaboratory CFD study problem statement also requested that participants calculate a corresponding relative index of hemolysis (RIH) at each condition:

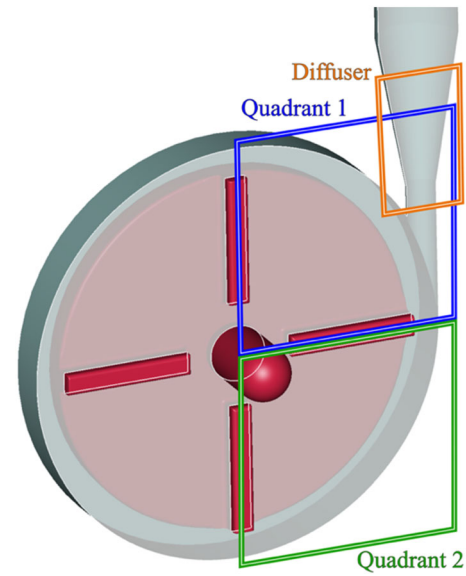


**FIGURE 2.** Illustration of the three data acquisition regions (Quadrant 1, Quadrant 2, and Diffuser) for the PIV measurements reported by Hariharan *et al.*<sup>16</sup> in the blade passage plane located 1.2 mm below the top surface of the rotor blades.

*“Please report a Relative Index of Hemolysis (RIH), defined as the ratio to the value you calculate at 6.0 L/min and 3500 RPM (to three significant digits). Thus the RIH at 6.0 L/min and 3500 RPM should be set equal to 1.00. This will allow us to compare indices regardless of method.”*

Unfortunately, however, there was some ambiguity in exactly how values of RIH should be calculated. For this reason, here we calculate RIH values from the experimental data using the two most common ways that interlaboratory CFD study participants could potentially have calculated this quantity. The first is simply calculated as:

$$RIH_{1,i} = \frac{fHb_i}{fHb_{6L/min, 3500rpm}} \quad (3)$$

where  $fHb_i$  is the absolute plasma free hemoglobin concentration at each condition and  $fHb_{6L/min, 3500rpm}$  is the value measured at the pump condition of 6 L/min and 3500 rpm (condition 5 in Table 1). The second definition of RIH is defined as:

$$RIH_{2,i} = \frac{MIH_i}{MIH_{6L/min, 3500rpm}} \quad (4)$$

where MIH is the modified index of hemolysis:

$$MIH = 10^6 \frac{(1 - H_{ct}/100)fHb}{Hb} \left( \frac{V}{Q\Delta t} \right) \quad (5)$$



Here,  $V$  is the total blood volume in the flow loop,  $Q$  is the volumetric flow rate,  $\Delta t$  is the time duration of the hemolysis experiment, and the conventional scaling factor of  $10^6$  is included so as to yield MIH values of reasonable magnitude.<sup>7,26</sup> The advantage of quantifying hemolysis data in terms of MIH is that it accounts for the blood hematocrit, the total blood hemoglobin concentration, and the number of passes of blood through the device in a multi-pass experiment. Additionally, it is closely related to the dimensionless hemolysis index that is used in one of the most popular hemolysis CFD models, the stress-based power law model (see Craven et al.<sup>7</sup> for details). Many interlaboratory CFD study participants used the hemolysis power law model and, thus, may have calculated RIH values based on MIH. Consequently, here we calculate both  $RIH_1$  and  $RIH_2$  from the experimental data and compare each with the CFD predictions submitted by the participants.

### Interlaboratory CFD Study

The interlaboratory CFD study was conducted by participants from around the world in a blinded fashion prior to the publication of the experimental data. The participants were only provided with the geometry of the pump, the nominal Newtonian blood properties of  $\rho = 1035 \text{ kg/m}^3$  and  $\mu = 3.5 \text{ cP}$  from the experiments, and the velocity profiles and turbulence intensities measured in the inflow tube at the location illustrated in Fig. 1b. Participants were asked to simulate the six pump operating conditions listed in Table 1. The participants were free to choose the specific CFD solver, mesh resolution, boundary conditions, turbulence model, and other simulation parameters. Participants were requested to submit specific scalar quantities of interest, such as the inlet and outlet pressures, shaft torque, and hemolysis predictions. Field data for pressure, velocity, and several other quantities were requested at specific locations, including the three key regions in the blade passage plane illustrated in Fig. 2. The field data were to be submitted with a blade oriented perpendicular to the outlet. Participants who performed transient simulations were requested to submit time-averaged results.

### Comparative Analysis

We performed a detailed analysis of the interlaboratory CFD study results submitted by all participants. To prevent the potential for bias, we anonymized the participant data prior to analysis. For the scalar quantities (pressure head and hemolysis), we analyzed the results for all pump operating conditions and calculated a percent error between the CFD and the

experimental measurements. For the velocity field, we performed both qualitative and quantitative comparisons. Due to the large amount of data, however, we restricted the velocity analysis to three pump operating conditions: (i) 2.5 L/min at 3500 rpm (condition 2), (ii) 6.0 L/min at 2500 rpm (condition 4), and (iii) 6.0 L/min at 3500 rpm (condition 5). These specific cases were chosen so as to explore the influence of changing pump flow rate at a fixed rotational speed and vice versa. At each condition, we compared the CFD velocity field predictions with the PIV measurements in the three key regions of the blade passage plane illustrated in Fig. 2 (Quadrant 1, Quadrant 2, and Diffuser).

Quantitatively comparing the velocity field between the different CFD simulations and the PIV measurements was complicated because each data set had a different spatial resolution. We, thus, created a high-resolution interpolation mesh onto which each of the data sets were interpolated using the Kriging interpolation tool available in the commercial post-processing software Tecplot 360 (version 2021 R1, Tecplot, Inc., Bellevue, WA, USA). The interpolation mesh is shown in the magnified inset of Fig. 3 and was generated using the commercial mesh generation software Pointwise (version 17.3, Pointwise, Inc., Fort Worth, TX). Importantly, to facilitate a high-quality interpolation, the mesh was created with wall-normal layers and with

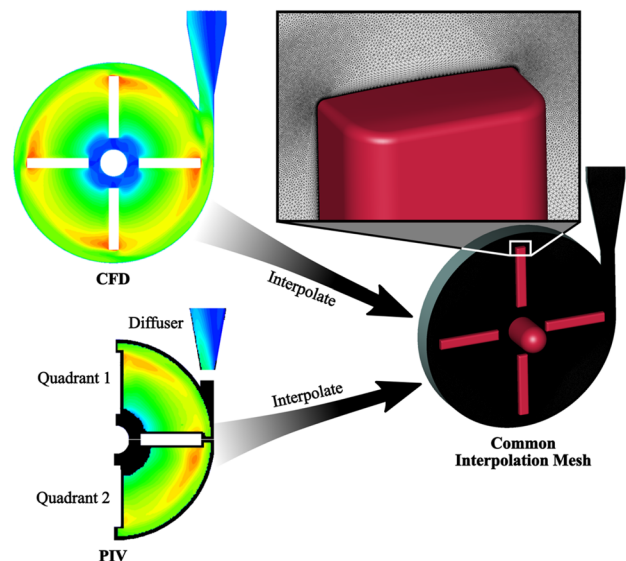


**FIGURE 3.** Schematic of the key data analysis steps for quantitatively comparing participant CFD simulation results with experimental PIV measurements by interpolating the velocity field data to a common high-resolution mesh. As illustrated by the black regions of the PIV data in the lower left panel, the analysis excluded data within 1 mm of the walls in the Quadrant 1 and Quadrant 2 regions and 0.15 mm from the walls in the Diffuser region due to the large experimental uncertainty in the PIV measurement of near-wall velocity.

an extremely high spatial resolution that was approximately six times greater than the finest CFD data set. As illustrated in Fig. 3, each of the participant CFD data sets and the PIV experimental data were interpolated to the nodes of this common mesh, allowing us to calculate the spatial distribution of the difference between CFD and PIV in each region. Because of the large uncertainty in the experimental data at the walls due to the challenges of accurately measuring near-wall velocity with PIV,<sup>33</sup> near-wall regions were excluded in this calculation. Specifically, we excluded data within 1 mm of the walls in the Quadrant 1 and Quadrant 2 regions and 0.15 mm from the walls in the Diffuser region, as shown by the black regions in the lower left panel of Fig. 3. Finally, to quantify the overall error in each CFD velocity field prediction compared with PIV, we calculated a percent global relative comparison error ( $\varepsilon$ ) for each region, defined as:<sup>8</sup>

$$\varepsilon = 100 \sqrt{\frac{1}{n} \sum_{i=1}^n \left( \frac{u_{\text{CFD},i} - u_{\text{PIV},i}}{\max(u_{\text{PIV}})} \right)^2} \quad (6)$$

where  $u_{\text{CFD},i}$  is the local CFD planar velocity magnitude at each mesh node,  $u_{\text{PIV},i}$  is the corresponding PIV value at the same location,  $\max(u_{\text{PIV}})$  is the maximum PIV value in the entire region of interest,  $n$  is the number of nodes in the interpolation mesh, and  $i$  represents the  $i$ th node.

## RESULTS

### Interlaboratory CFD Study Participant Submissions

In total, there were 24 interlaboratory study submissions from 23 participants using a wide range of CFD flow solvers, reference frame formulations, turbulence models, and meshes. An overall summary of the submissions is provided in Table 2, and Table 3 lists the methodological details of each individual participant

submission. All participants used commercial CFD solvers, except for one who used the open-source software *code\_saturne*. Of the 24 submissions, 14 simulated steady-state flow using a multi-reference frame formulation and a frozen rotor approach with the rotor stationary and a blade oriented perpendicular to the outlet. Only 10 of 24 submissions simulated the transient flow due to the rotation of the rotor using a sliding mesh interface. One participant (participant 3) submitted both steady-state and transient simulation results, denoted here as submissions ‘3s’ and ‘3t’, respectively (see Table 3). The  $k-\omega$  shear-stress transport (SST) turbulence model was the most popular choice (13 participants), followed by different variants of the  $k-\varepsilon$  model (standard [3], realizable [3], and RNG [1]) and the one-equation Spalart–Allmaras model (2). One participant used the  $R_{ij}-\varepsilon$  SSG Reynolds stress model.

As illustrated in Fig. 4, the interlaboratory study participants used a wide range of different types of computational meshes. Two-thirds of the submissions (16 of 24) used a tetrahedral-based mesh, and four each used hexahedral and polyhedral mesh topologies. The resolution of the CFD meshes ranged widely, from rather coarse (about 530 thousand computational cells) to very fine (76.5 million computational cells).

Only one-third of the CFD submissions (8 of 24) included predictions of hemolysis. This is likely because commercial and open-source CFD software generally do not provide hemolysis models, requiring users to implement their own model of choice. Of the three participants who reported the details of their hemolysis model implementation, one implemented their model with custom code in a commercial CFD solver environment and the other two used the CFD solver flow solution with a hemolysis model that was implemented as custom software, external to the CFD flow solver. All but one of the participants who submitted hemolysis results used the popular stress-based power law model<sup>7</sup> (see Table 3), while the remaining participant used the strain-based model of Pauli *et al.*<sup>30</sup>

TABLE 2. Summary of interlaboratory CFD study submissions.

Simulation option	Participant submissions (24)
CFD solver	Abaqus/CFD (1), AcuSolve (2), ANSYS CFX (6), ANSYS Fluent (7), <i>code_saturne</i> (1), FlowVision (1), SC/Tetra (1), STAR-CCM+ (5)
Time integration	Steady (14), Transient (10)
Turbulence model	$k-\omega$ SST (13), Standard $k-\varepsilon$ (3), Realizable $k-\varepsilon$ (3), Spalart–Allmaras (2), RNG $k-\varepsilon$ (1), $R_{ij}-\varepsilon$ SSG (1), not provided (1)
Hemolysis model	Lagrangian stress-based power law (2), Eulerian stress-based power law (4), Unspecified stress-based power law (1), Strain-based model of Pauli <i>et al.</i> <sup>30</sup> (1)
Mesh topology	Tetrahedral (16), Hexahedral (4), Polyhedral (4)
Num cells ( $\times 10^6$ )	Min: 0.53, Max: 76.5, Mean: 11.6, Median: 9.4
Num nodes ( $\times 10^6$ )	Min: 0.42, Max: 60.7, Mean: 9.9, Median: 2.8

The number of submissions for each category are denoted in parentheses.

**TABLE 3. Details of individual interlaboratory CFD study participant submissions.**

Participant #	Time integration	Turbulence model	Hemolysis model	Mesh topology	Num Cells ( $\times 10^6$ )	Num Nodes ( $\times 10^6$ )	Blade mesh $y^+$
1	Steady	k- $\omega$ SST	L power law	tet	2.2	0.42	*
2	Transient	Realizable k- $\epsilon$	E power law	poly	11.1	*	0.5–1.4
3s	Steady	k- $\omega$ SST	E power law	tet	18.5	7.0	1.3–2.0
3t	Transient	k- $\omega$ SST	–	tet	18.5	7.0	1.3–2.0
4	Steady	Spalart–Allmaras	strain-based	tet	10.9	1.9	2.0
5	Steady	k- $\omega$ SST	ukn power law	tet	8.0	2.9	0.5–0.6
6	Steady	k- $\omega$ SST	–	tet	8.7	2.5	1.5–2.2
7	Transient	RNG k- $\epsilon$	–	hex	10.1	10.5	*
8	Steady	Realizable k- $\epsilon$	–	tet	10.7	3.7	0.9–1.4
9	Transient	Standard k- $\epsilon$	–	hex	1.6	1.5	1.3–1.9
10	Transient	R <sub>ij</sub> - $\epsilon$ SSG	–	tet	76.5	12.1	*
11	Transient	k- $\omega$ SST	L power law	hex	19.1	18.9	1.9–2.6
12	Transient	Standard k- $\epsilon$	–	hex	0.53	*	9.9–13.6
13	Steady	k- $\omega$ SST	–	poly	3.4	11.8	1.5
14	Steady	k- $\omega$ SST	E power law	tet	11.6	3.1	0.9–1.3
15	Steady	k- $\omega$ SST	–	tet	8.2	2.4	1.5–2.1
16	Steady	Standard k- $\epsilon$	–	tet	4.1	1.0	4.5–6.0
17	Steady	k- $\omega$ SST	–	tet	5.7	2.0	0.05–3.1
18	Steady	Realizable k- $\epsilon$	–	poly	2.7	*	1.0–1.8
19	Transient	Spalart–Allmaras	–	tet	15.7	2.8	0.6–0.8
20	Transient	k- $\omega$ SST	–	tet	2.2	0.68	2.3–3.1
21	Steady	k- $\omega$ SST	–	tet	10.8	2.6	0.8–1.6
22	Transient	k- $\omega$ SST	–	tet	5.7	2.0	0.05–3.1
23	Steady	Unknown	E power law	poly	11.1	*	0.4–0.6

L power law: Lagrangian stress-based power law; E power law: Eulerian stress-based power law; strain-based: strain-based model of Pauli et al.<sup>30</sup>; ukn power law: unspecified stress-based power law; tet: tetrahedral; poly: polyhedral; hex: hexahedral.

–Hemolysis result not reported.

\*Suspected reporting error or not reported.

### Pressure Head

A comparison of the CFD predictions with the pump pressure head measurements acquired during the PIV experiments is shown in Fig. 5, where we have omitted CFD results at a single operating condition for three participants due to suspected reporting errors (e.g., reporting of a negative pressure head). In general, most of the CFD predictions were within two standard deviations of the mean experimental data, except for the 6.0 L/min, 2500 rpm case (condition 4) for which only 16 of the submissions were within this range (Fig. 5a). Of the 24 CFD submissions, 10 of the participants (2, 3s, 4, 6, 13–16, 19, and 21) accurately predicted the pressure head within two standard deviations of the experimental mean at all six pump operating conditions. As shown in Fig. 5b for conditions 4 and 5, there is not a strong correlation of CFD percent error in the predicted pump pressure head with mesh resolution, quantified here in terms of the number of computational cells. Though not shown, the same is true for the other operating conditions and also when the results are plotted as a function of the number of mesh nodes.

Examining the influence of turbulence model, there were three models that generally performed the best for

predicting the pressure head across all conditions. The average predictions from the k- $\omega$  SST, realizable k- $\epsilon$ , and Spalart–Allmaras models were all within two standard deviations of the mean experimental data at all six operating conditions, whereas average predictions from the other turbulence models were outside of this range for at least one condition. Among these three top-performing models, the realizable k- $\epsilon$  and Spalart–Allmaras models had similar percent errors at most conditions that were slightly less than the k- $\omega$  SST model (Fig. 5c).

The influence of steady versus transient simulation type is plotted in Fig. 5d. Here, we see that participants who simulated steady-state flow using a multi-reference frame formulation and a frozen rotor approach generally predicted values of the pump pressure head that had similar percent errors compared to those participants who simulated transient flow with the rotor rotating.

### Velocity Field

Figures 6, 7, and 8 show comparisons of the planar velocity magnitude contours from each of the available CFD predictions with the PIV measurements for conditions 2, 4, and 5, respectively. In each case, we omitted any participant with data reporting errors

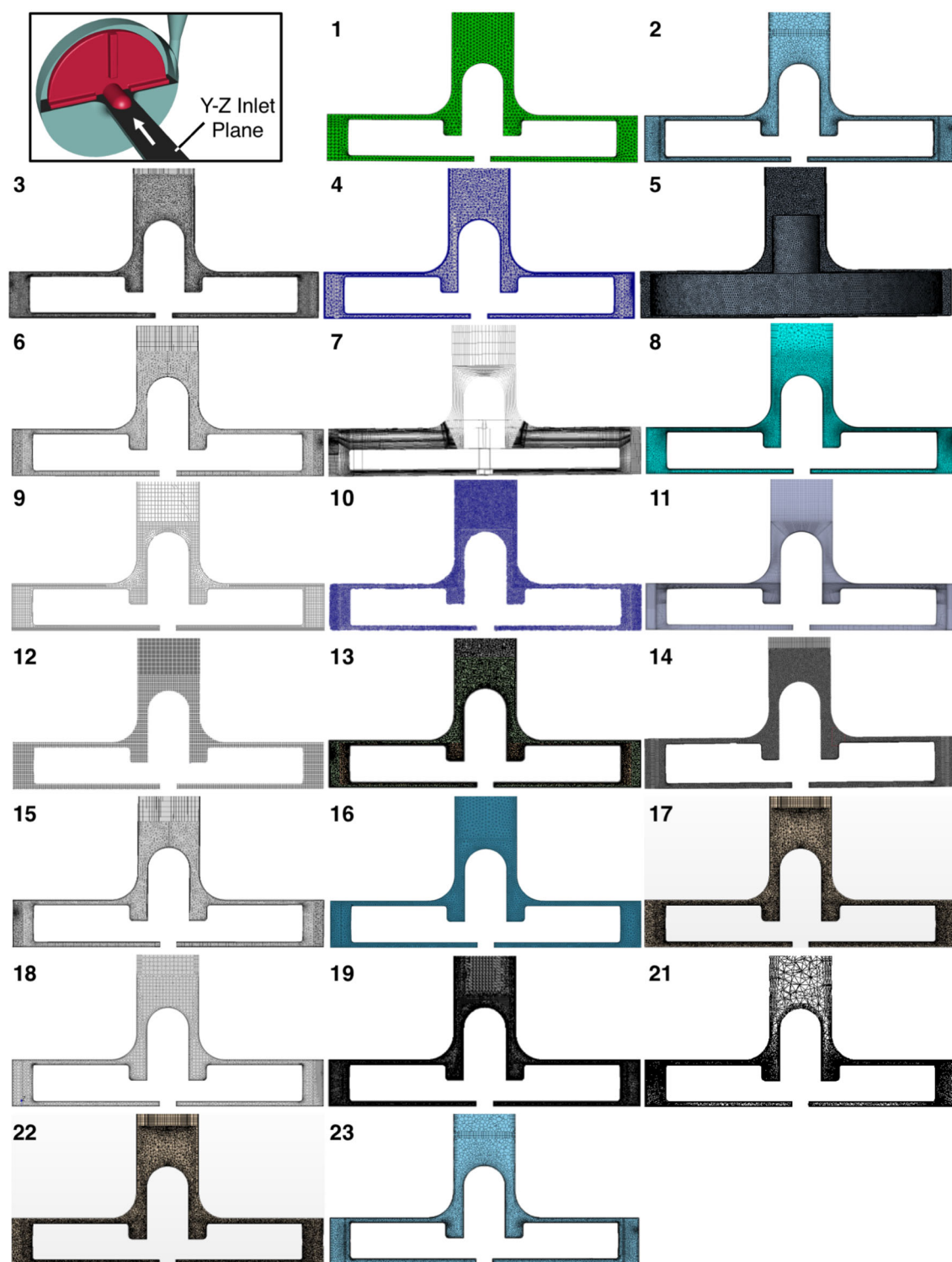
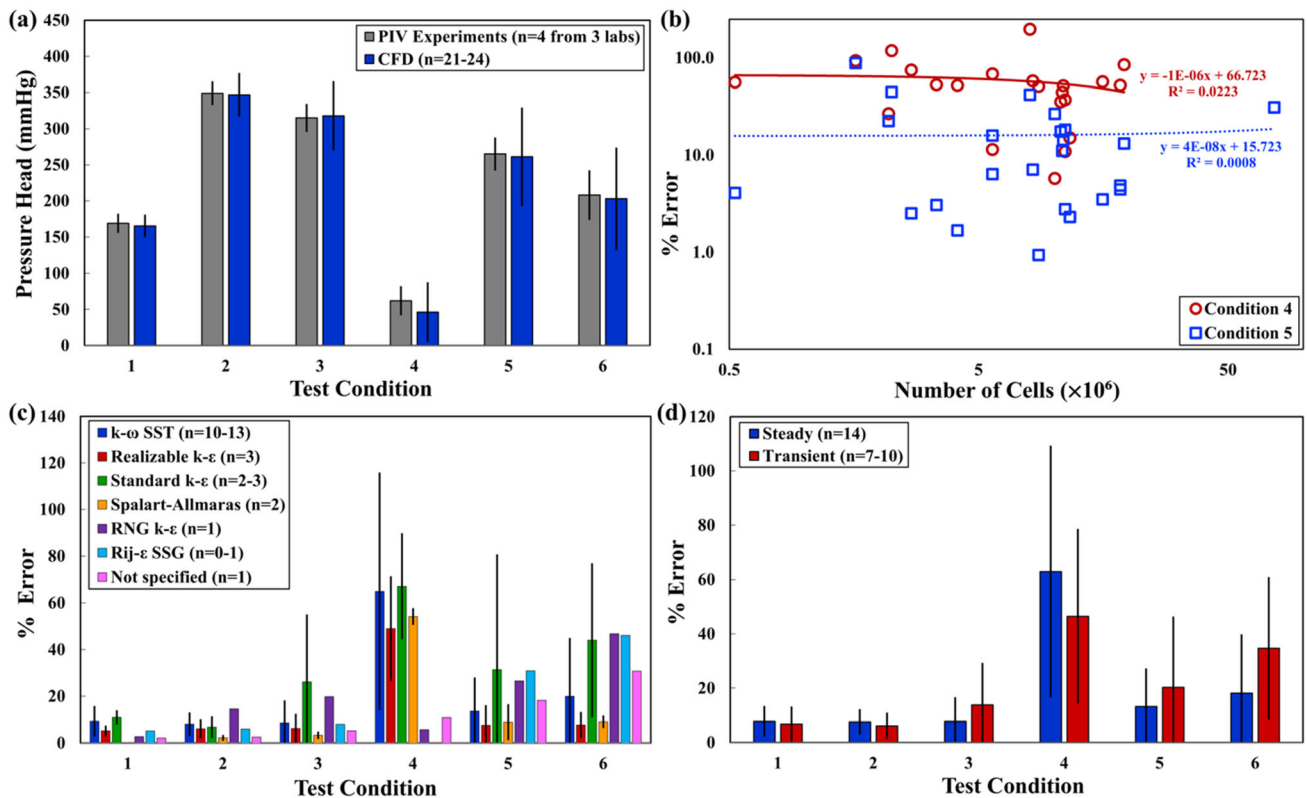


FIGURE 4. Cross-section in the Y-Z inlet plane through the computational meshes used by the interlaboratory CFD study participants.





**FIGURE 5.** CFD pump pressure head predictions compared with experimental measurements. (a) Summary of the pump pressure head from interlaboratory CFD study simulations and interlaboratory PIV experiments in three labs. (b) Percent error in the CFD results as a function of mesh resolution quantified in terms of the number of computational cells for conditions 4 and 5. (c) CFD percent error as a function of turbulence model. (d) CFD percent error for steady versus transient simulations. Where present, error bars represent mean  $\pm$  SD.

(e.g., several transient CFD submissions were with the rotor blade not oriented perpendicular to the outlet as requested). For condition 2, within quadrant 1 of the rotor region, all submissions except participant 1 predicted similar qualitative velocity distributions with the highest velocity around and just downstream of the blade tip (Fig. 6). All participants predicted that a jet forms in the diffuser that is skewed (to varying degrees) toward the inner wall, which generally agrees with PIV. For condition 4 (Fig. 7), the PIV measurements show a region of high-velocity flow extending to the rotor housing in quadrant 1. All of the transient CFD submissions predict qualitatively similar high-velocity flow in this region, whereas none of the steady CFD submissions predict this flow feature. With the exception of participant 1, all of the CFD submissions predict a jet in the diffuser that is skewed to vary degrees toward that outer wall for condition 4, as observed in the PIV measurements. Finally, for condition 5 (Fig. 8), except for participant 1, all of the CFD submissions predict similar qualitative velocity fields within quadrant 1 with the highest velocity around and just downstream of the blade tip. In the diffuser, however, there was more variability in the CFD predictions. The PIV data

show that the jet in the diffuser is slightly skewed toward the outer wall. All of the transient CFD submissions predict this outward skewness of the jet, whereas several of the steady submissions (from participants 1, 14, 21, and 23) do not.

The quantitative CFD comparison error ( $\epsilon$ ) for each of the participants is summarized in Fig. 9. As for pressure, the velocity error was not generally correlated with the mesh resolution. The largest velocity errors for most of the participants occurred in the diffuser for all three conditions (Figs. 9a–c). In the rotor region, most CFD submissions had comparable error in quadrants 1 and 2 for condition 2 (Fig. 9a), but for the higher flow rate conditions 4 and 5 many of the submissions had a larger error in quadrant 1 than in quadrant 2 (Figs. 9b, c). Comparing transient versus steady CFD simulations, the transient results generally agreed more closely with PIV within the rotor region of the pump compared to steady CFD (Figs. 9d–f). In the diffuser, however, the transient and steady CFD predictions were more comparable.

The influence of turbulence model is plotted in Fig. 10. In the rotor region, the velocity errors were comparable for most of the turbulence models, except

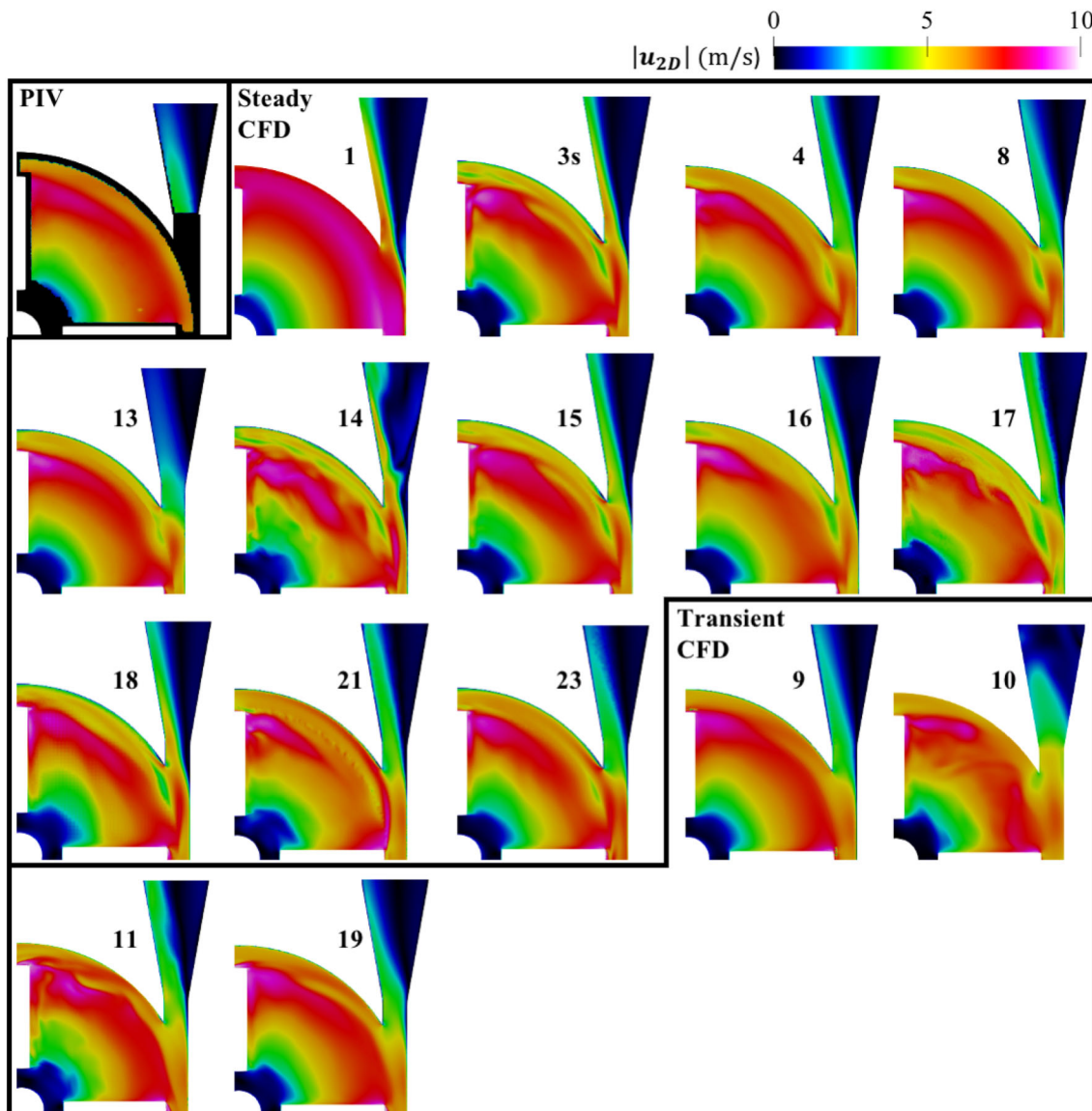


FIGURE 6. Comparison of planar velocity magnitude contours from PIV and CFD for condition 2 (2.5 L/min, 3500 rpm).

in quadrant 1 for conditions 4 and 5 (Figs. 10b, 10c). At these conditions, the RNG  $k-\varepsilon$  and  $R_{ij}-\varepsilon$  SSG models performed slightly better than the rest, though this observation is based on results from a single participant using each model. In the diffuser, the realizable  $k-\varepsilon$  and Spalart–Allmaras turbulence models generally performed the best across all three analyzed conditions.

### Hemolysis

A comparison of the CFD results with the experimental measurements of fHb is shown in Fig. 11a, where we have omitted results from two participants due to suspected reporting errors. As shown, one CFD

submission (participant 1) successfully predicted the absolute levels of fHb within one SD of the mean experimental data across all pump operating conditions. Of the 30 total CFD hemolysis predictions submitted for all of the test conditions by the other five participants plotted in Fig. 11a, only eight were within one SD of the experimental data. All other CFD hemolysis predictions were outside of this range, many by an order of magnitude or more.

Participants were generally more successful at predicting experimental values of RIH than they were at predicting absolute hemolysis levels. In Fig. 11b, we plot  $RIH_1 = fHb/fHb_5$  for the three participants who reported values of RIH that were clearly calculated in this fashion based on their reported levels of fHb.

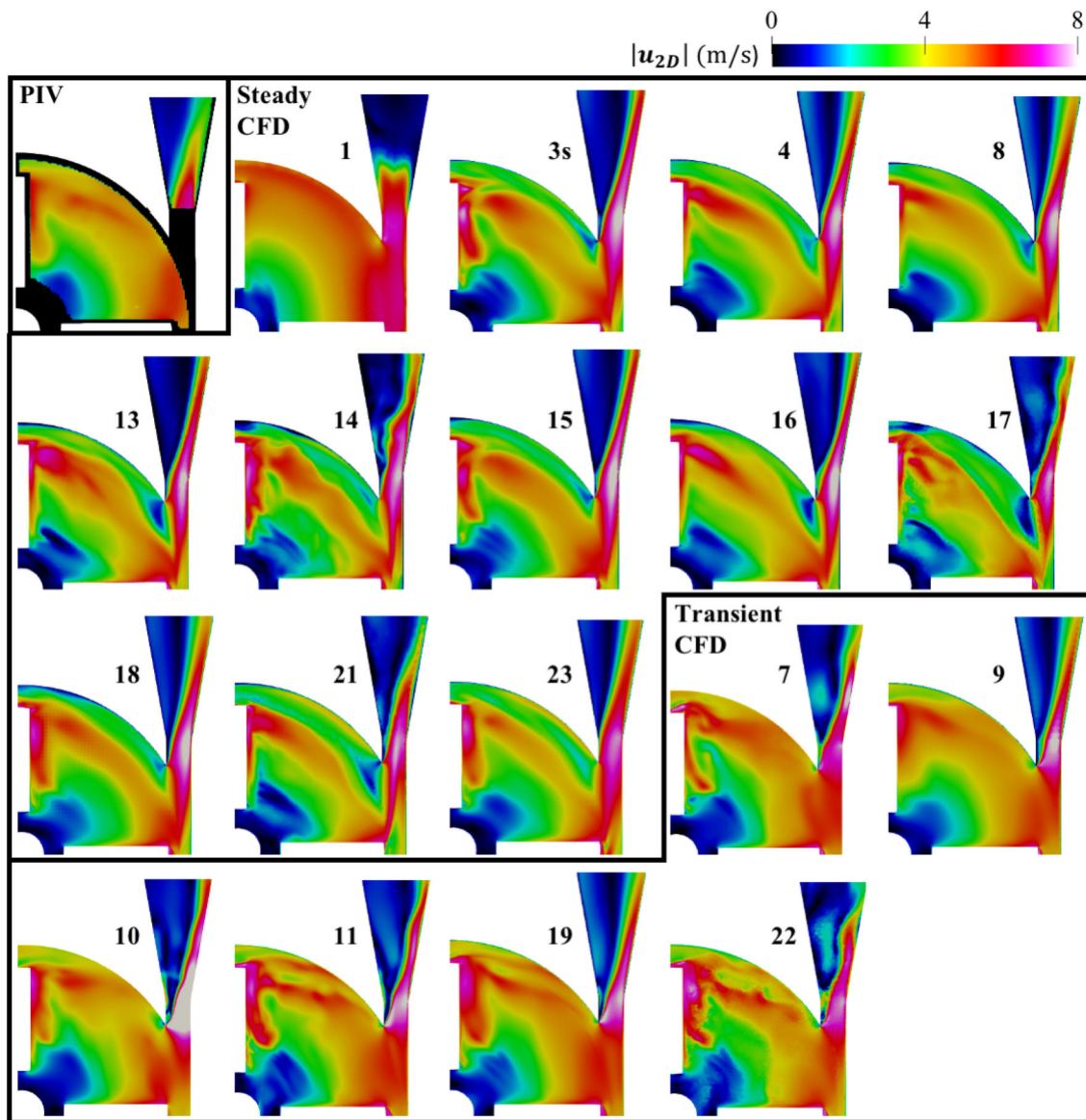


FIGURE 7. Comparison of planar velocity magnitude contours from PIV and CFD for condition 4 (6.0 L/min, 2500 rpm).

Here, we see that two participants (1 and 11) accurately predicted  $RIH_1$  within one SD of the mean experimental data at all of the pump operating conditions. In Fig. 11c, we plot  $RIH_2 = MIH/MIH_5$  for the remaining five participants who reported values of  $RIH$  that were clearly not calculated based on their reported levels of  $fHb$ . We used this secondary definition of  $RIH$  because most of these participants used the hemolysis power law model, which is formulated in terms of a dimensionless index that is closely related to  $MIH$  (see Craven et al.<sup>7</sup> for details). Given that there was some ambiguity in the original interlaboratory CFD study problem statement on exactly how  $RIH$  should be calculated, it is likely that these participants may have calculated it based on  $MIH$  predictions.

From Fig. 11c, we see that two of the participants (3s and 14) predicted values of  $RIH_2$  that are within one SD of the mean experimental measurements in all cases. Overall, 20 of the 25 CFD hemolysis predictions submitted by the five participants in Fig. 11c were within one SD of the mean experimental  $RIH_2$ .

## DISCUSSION

The development and validation of improved CFD predictive models will lead to better tools for designing and evaluating medical devices, not only for performance but also with regards to blood damage safety (e.g., hemolysis, platelet activation, thrombosis, von



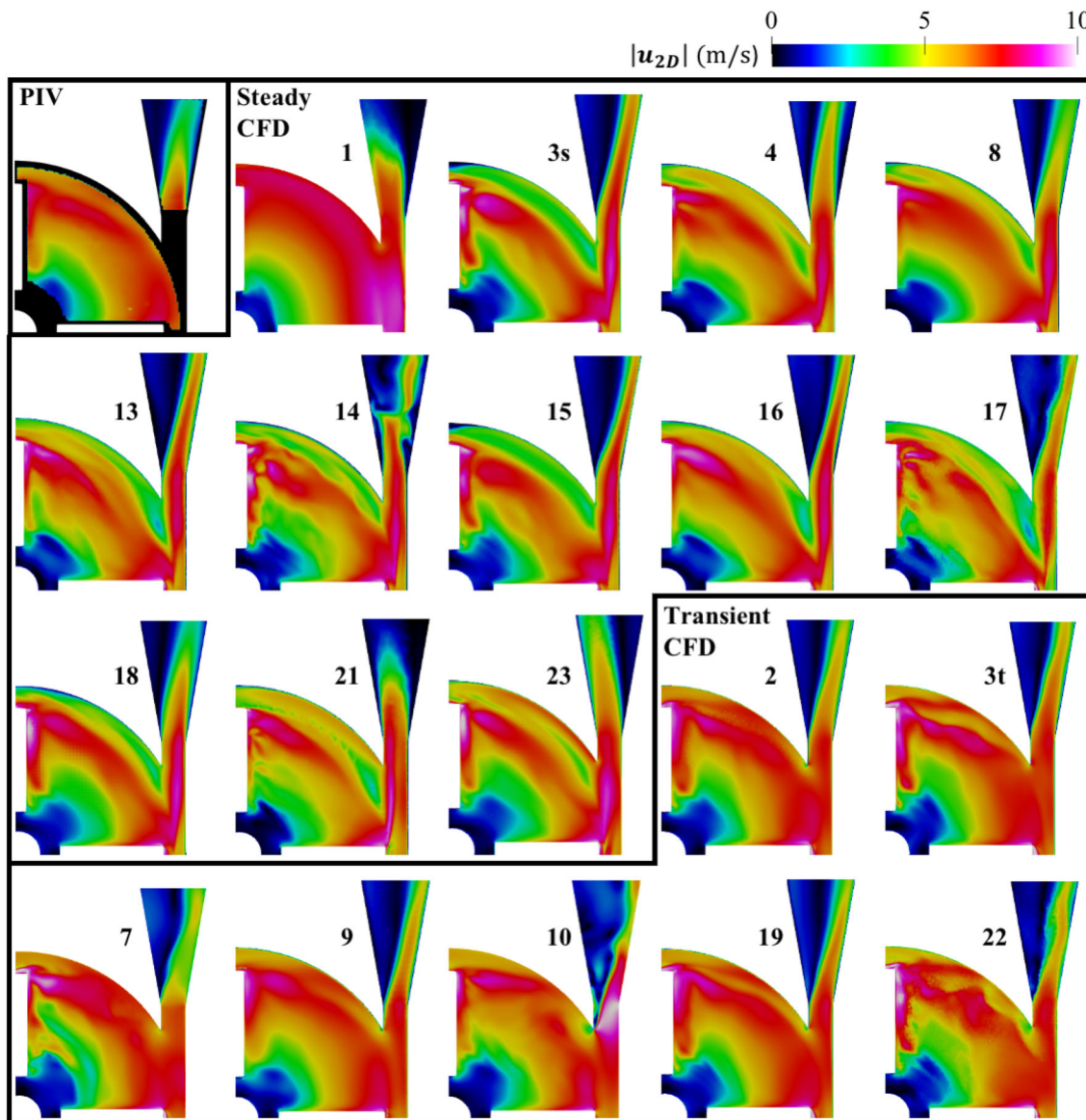


FIGURE 8. Comparison of planar velocity magnitude contours from PIV and CFD for condition 5 (6.0 L/min, 3500 rpm).

Willebrand factor damage). In this study, we report the results of the interlaboratory CFD study of the FDA benchmark blood pump. We analyzed the results of 24 CFD submissions by participants from around the world who used different flow solvers, mesh topologies and resolutions, time integration schemes, and turbulence models. To assess the accuracy of the CFD predictions, we compared the results with experimental measurements of the pressure head, velocity fields, and hemolysis at several different pump conditions spanning the entire operating range of the device.

In general, though a number of CFD submissions accurately predicted the pump performance for individual cases, no single participant was able to accurately predict all quantities of interest (pressure head,

velocity, and hemolysis) at all conditions. Of the 24 CFD submissions, 10 participants (2, 3s, 4, 6, 13–16, 19, and 21) accurately predicted the pressure head within two standard deviations of the experimental mean values for all six operating conditions. As summarized in Table 4, however, none of these participants accurately predicted the velocity magnitude in all regions to within 20% of the PIV data at all conditions. The velocity field predictions from participant 4 were all within 20% of the PIV data, except for condition 4 in the diffuser, which had an error of 20.9%. Similarly, the velocity predictions from participants 14, 19, and 21 were all within 20% of the PIV data, except in two cases each (see Table 4). Finally, though the velocity errors for conditions 2 and 4 were not quan-



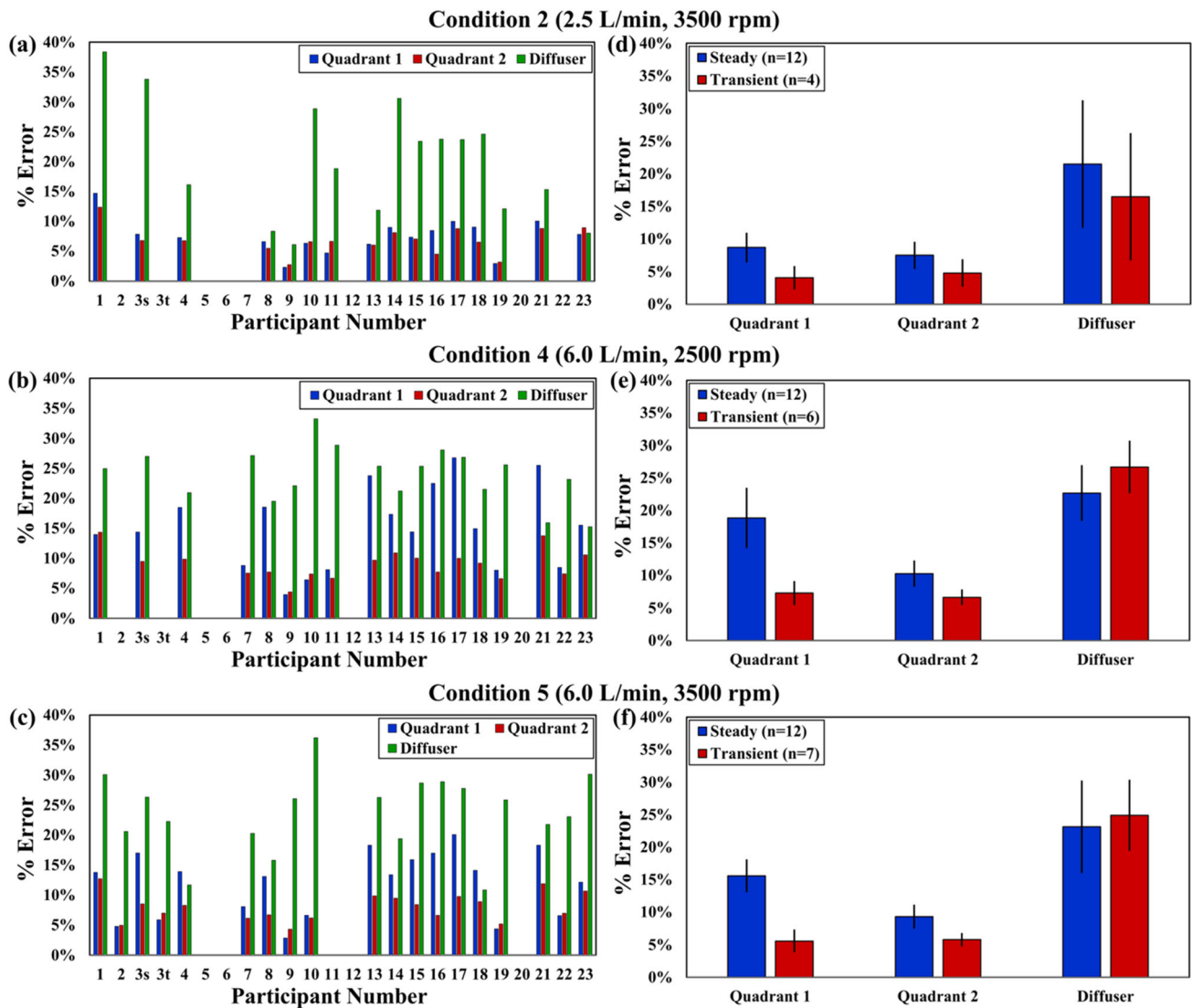


**FIGURE 9.** Percent global relative comparison error ( $\varepsilon$ ) (Eq. 6) for the CFD predictions of planar velocity magnitude compared with PIV measurements. (a–c) Summary of the comparison error for all available participants in quadrant 1, quadrant 2, and the diffuser regions of the pump for operating conditions of (a) 2.5 L/min at 3500 rpm (condition 2), (b) 6.0 L/min at 2500 rpm (condition 4), and (c) 6.0 L/min at 3500 rpm (condition 5). (d–f) Comparison error of steady versus transient CFD simulations for (d) condition 2, (e) condition 4, and (f) condition 5.

tified for participant 2 due to a reporting error (they submitted data with a rotor blade not oriented perpendicular to the outlet as requested), their predictions of the velocity field for condition 5 were generally quite good, with errors of approximately 5% in the rotor region and 20.6% in the diffuser. Of these five overall top participants (2, 4, 14, 19, and 21), three submitted hemolysis results (participants 2, 4, and 14). As noted in Table 4, participants 2 and 4 predicted absolute levels of fHb within one SD of the mean experimental data at two conditions each and RIH values within this range at three and four conditions, respectively. While participant 14 had a suspected error in their reporting

of fHb, they successfully predicted RIH values within one SD of the experiments at all conditions.

Comparing the CFD methodologies used by these five overall top participants (2, 4, 14, 19, and 21), there are some similarities. From Table 3 we see that three of these participants (4, 14, and 21) simulated steady-state flow while participants 2 and 19 performed more computationally expensive transient flow simulations. Two of the participants (14 and 21) used the  $k-\omega$  SST turbulence model, two others (participants 4 and 19) used the Spalart–Allmaras model, and participant 2 used the realizable  $k-\varepsilon$  model. Four of the participants (4, 14, 19, and 21) used a moderately fine tetrahedral-

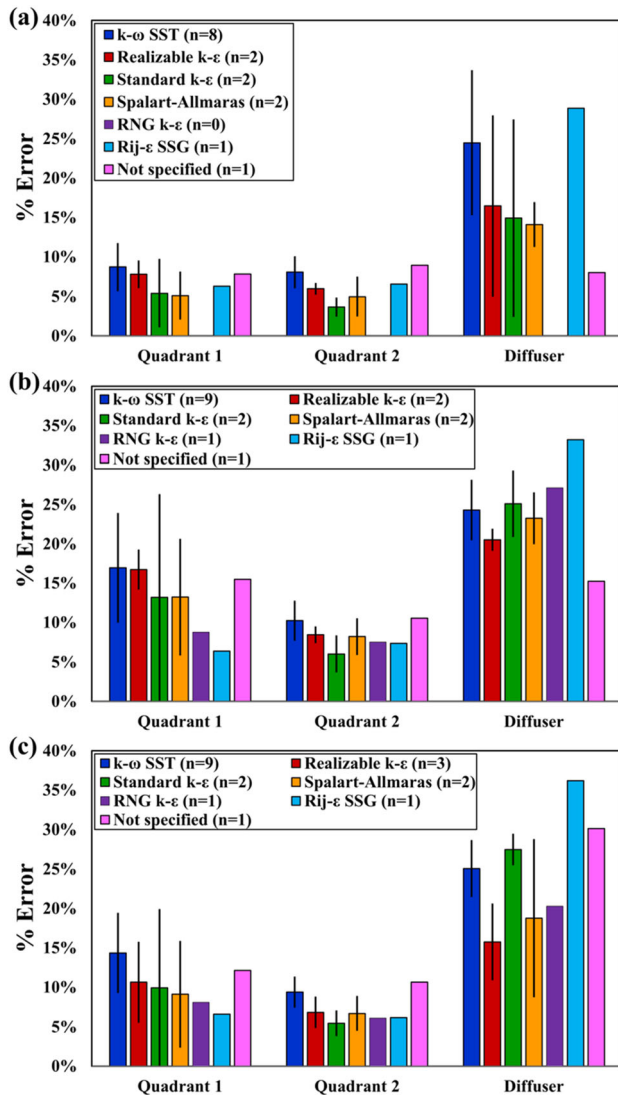


FIGURE 10. Percent global relative comparison error ( $\epsilon$ ) (Eq. 6) for the CFD predictions of planar velocity magnitude as a function of turbulence model for (a) condition 2, (b) condition 4, and (c) condition 5.

based CFD mesh with about 11–16 million computational cells and the other participant (2) used a polyhedral mesh with 11 million computational cells.

It is also interesting to note the accuracy of the hemolysis predictions of participant 1 considering the overall inaccuracy of their pressure and velocity predictions. Remarkably, participant 1 accurately predicted both the absolute and relative levels of hemolysis at all pump operating conditions. They, however, significantly over-predicted the pump pressure head at all conditions, having no prediction within two standard deviations of the mean experimental data. Their predictions of the velocity field for the three analyzed conditions were also relatively inaccurate in many cases. It is, thus, curious as to why their

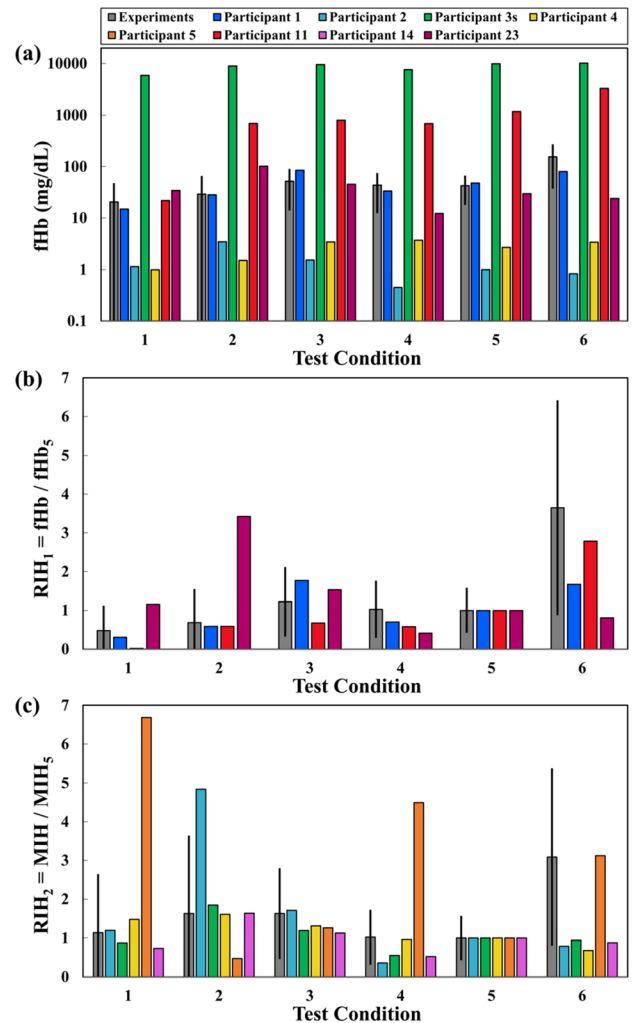


FIGURE 11. CFD hemolysis predictions compared with experimental measurements (mean  $\pm$  SD) for the (a) absolute plasma free hemoglobin concentration (fHb), (b) relative index of hemolysis ( $RIH_1$ ) calculated in terms of fHb, and (c)  $RIH_2$  calculated in terms of the modified index of hemolysis (MIH).

hemolysis predictions are so remarkably accurate. We speculate that it may be coincidental and due to the fortunate selection of model coefficients for the hemolysis power law model, which is entirely empirical and can yield an extremely wide range of predictions depending on the specific coefficients that are used.<sup>7</sup>

We also analyzed the influence of different CFD methods and modeling choices used by the participants. While the number of participants using different options and approaches was insufficient to determine definitive trends, we made some valuable observations. Notably, CFD accuracy was not strongly correlated with the resolution of the computational mesh. We, however, caution that this does not imply that CFD accuracy is independent of mesh resolution in general, as numerical discretization error should diminish as

**TABLE 4. Summary of velocity and hemolysis results for the 10 interlaboratory CFD study participants who successfully predicted the pump pressure head within two standard deviations of the mean experimental data.**

Participant #	Velocity (% error)									Hemolysis (within $\pm 1$ SD of mean exp data: y/n)					
	Quadrant 1			Quadrant 2			Diffuser			fHb/RIH					
	C2	C4	C5	C2	C4	C5	C2	C4	C5	C1	C2	C3	C4	C5	C6
2	*	*	<b>4.7</b>	*	*	<b>4.9</b>	*	*	20.6	y/y	y/n	n/y	n/y	n	n/n
3s	<b>7.8</b>	<b>14.4</b>	<b>17.0</b>	<b>6.7</b>	<b>9.4</b>	<b>8.5</b>	33.8	27.0	26.3	n/y	n/y	n/y	n/y	n	n/y
4	<b>7.2</b>	<b>18.5</b>	<b>13.9</b>	<b>6.7</b>	<b>9.8</b>	<b>8.2</b>	<b>16.1</b>	20.9	<b>11.7</b>	y/y	y/y	n/y	n/y	n	n/n
6	*	*	*	*	*	*	*	*	*	—	—	—	—	—	—
13	<b>6.2</b>	23.8	<b>18.3</b>	<b>6.0</b>	<b>9.6</b>	<b>9.8</b>	<b>11.9</b>	25.4	26.3	—	—	—	—	—	—
14	<b>9.0</b>	<b>17.3</b>	<b>13.4</b>	<b>8.1</b>	<b>10.9</b>	<b>9.5</b>	30.6	21.2	<b>19.4</b>	*y	*y	*y	*y	*	*y
15	<b>7.3</b>	<b>14.4</b>	<b>15.9</b>	<b>7.0</b>	<b>10.0</b>	<b>8.4</b>	23.4	25.3	28.7	—	—	—	—	—	—
16	<b>8.5</b>	22.5	<b>17.0</b>	<b>4.5</b>	<b>7.7</b>	<b>6.6</b>	23.8	28.1	28.9	—	—	—	—	—	—
19	<b>3.0</b>	<b>8.0</b>	<b>4.3</b>	<b>3.2</b>	<b>6.6</b>	<b>5.1</b>	<b>12.1</b>	25.6	25.9	—	—	—	—	—	—
21	<b>10.0</b>	25.5	<b>18.3</b>	<b>8.8</b>	<b>13.8</b>	<b>11.9</b>	<b>15.3</b>	<b>15.9</b>	21.8	—	—	—	—	—	—

For velocity, the percent relative error ( $\varepsilon$ ) (Eq. 6) is provided in each pump region. For hemolysis, 'y' or 'n' indicates whether or not the CFD prediction was within one SD of the experimental mean value for absolute (fHb) or relative (RIH) quantities.

C1–C6 denote pump operating conditions 1–6, respectively.

\*Suspected reporting error.

—Hemolysis result not reported.

Bold italics indicates  $< 20\%$  velocity error.

the CFD mesh is refined. The lack of correlation of CFD accuracy with mesh resolution observed in this study is likely due to the large variability of the numerical methods (finite volume, finite element), mesh types (tetrahedral, polyhedral, hexahedral), turbulence models, and reference frame formulations that were used by the various participants. These other modeling choices also contribute to the numerical accuracy, making it difficult to separate out their individual contributions and to determine definitive trends.

Investigating the influence of turbulence model, we found that there were three models ( $k-\omega$  SST, realizable  $k-\varepsilon$ , and Spalart–Allmaras) that generally performed the best for predicting the pressure head across all conditions. Two of those models (realizable  $k-\varepsilon$  and Spalart–Allmaras) generally also performed well for predicting the velocity field, particularly within the diffuser. Comparing steady versus transient simulation type, transient CFD predictions of the velocity field in the rotor region were generally more accurate than steady CFD predictions. But, otherwise, the results for the pressure head and the velocity field in the diffuser were generally comparable between steady and transient CFD.

Overall, this study highlights the need to validate CFD modeling of rotary blood pumps across the entire range of operating conditions and for all quantities of interest. Such extensive validation is needed because some conditions and regions are more challenging to predict than others, as shown here for condition 4 and

the diffuser region of the FDA blood pump. All quantities of interest should be validated because, as demonstrated here with participant 1, it is possible to accurately predict hemolysis despite having relatively inaccurate predictions of the flow field.

There are, however, several limitations of the study. Due to the open interlaboratory study design, we were unable to rigorously quantify the influence of different modeling approaches and options on the predictive accuracy of CFD. Doing so would require a study that is specifically designed to systematically examine the accuracy of CFD predictions using different modeling options, which was outside the scope of the present study. But, it is an area of interest for future work that is needed in order to establish best practices for CFD modeling of blood pumps. Toward this end, to enable the broad dissemination of research by others in this area, at our website repository ([https://ncihub.org/wiki/FDA\\_CFD/ComputationalRoundRobin1Nozzle/citations](https://ncihub.org/wiki/FDA_CFD/ComputationalRoundRobin1Nozzle/citations)) we have included a list of published studies that have used the FDA benchmark nozzle and blood pump data to evaluate and improve CFD applied to medical devices.

Also, our validation of the flow field in this study was confined to comparing with PIV measurements of the planar velocity magnitude in three regions of the pump. We did not validate turbulence predictions and, due to practical limitations with analyzing such a large amount of data, we did not consider comparisons of velocity components and we only compared CFD predictions to PIV data in quadrants 1 and 2 in the

rotor region and in the diffuser. While the flow in these three regions is critical to understanding the pump performance, the fluid dynamics in some other regions of the pump may also be important. Future work should investigate ways to measure the full three-dimensional mean velocity and turbulence fields in all regions of the pump (e.g., using magnetic resonance velocimetry<sup>10,11,23</sup>) for direct comparison with volumetric field predictions from CFD.

Additionally, the PIV experiments and the CFD simulations in this study utilize a Newtonian blood analog fluid, whereas the hemolysis experiments used whole blood, which is non-Newtonian. Though blood behaves as Newtonian at high strain rates, the extent to which non-Newtonian blood rheology affects the flow field in the benchmark centrifugal blood pump has yet to be experimentally investigated. The potential influence of non-Newtonian effects is a common challenge when interpreting PIV and CFD results of blood flow using Newtonian blood analogues. A recent CFD study<sup>14</sup> of the FDA blood pump found that non-Newtonian effects are small at high flow rate conditions (conditions 4 and 5), but have a greater influence at the low flow rate and low rotational speed case of condition 1. There are no experimental data, however, to validate the non-Newtonian flow predictions. Future experimental flow studies should investigate using non-Newtonian blood analog fluids for PIV<sup>27</sup> or even whole blood with magnetic resonance velocimetry.<sup>10,11,23</sup> This is important to consider because non-Newtonian effects may have some influence on blood damage, especially thrombosis. While hemolysis typically occurs in regions of high strain rate where blood likely behaves as Newtonian, thrombosis usually occurs in regions of low-speed or stagnant flow, where non-Newtonian effects are more significant.

Finally, it is important to emphasize that this work is the result of a collaboration between government, academic, and industry researchers who planned and participated in the FDA-sponsored interlaboratory CFD and experimental studies. Thanks to their combined efforts, the results of the FDA benchmark nozzle and blood pump studies have impacted the development of the ASME V&V 40-2018 standard (“Assessing Credibility of Computational Modeling Through Verification and Validation: Application to Medical Devices”)<sup>1</sup> and an FDA Guidance Document<sup>12</sup> for reporting critical aspects of computational modeling studies in medical device regulatory submissions to the FDA. Moreover, the benchmark datasets are being widely used by other researchers to evaluate and improve CFD modeling of medical devices (e.g., see [https://ncihub.org/wiki/FDA\\_CFD/ComputationalRoundRobin1Nozzle/citations](https://ncihub.org/wiki/FDA_CFD/ComputationalRoundRobin1Nozzle/citations)) and even to train the next generation of computational scientists in academia.

## ACKNOWLEDGMENTS

We thank Dr. Steven Day of the Rochester Institute of Technology who helped to design and fabricate the blood pump model in collaboration with RAM, and Dr. Sandy Stewart of the FDA for administering the interlaboratory CFD study. We thank Dr. Kenneth Aycock for reviewing the manuscript and for providing helpful comments and suggestions. This project was funded by the FDA CDRH Critical Path program and, in part, by a National Science Foundation INTERN supplement through NSF CMMI-2017805.

## CONFLICT OF INTEREST

The authors declare that they have no conflicts of interest.

## REFERENCES

- <sup>1</sup>ASME V&V 40-2018. Assessing Credibility of Computational Modeling Through Verification and Validation: Application to Medical Devices. New York, NY: American Society of Mechanical Engineers, 2018.
- <sup>2</sup>Aycock, K. I., R. L. Campbell, F. C. Lynch, K. B. Manning, and B. A. Craven. The importance of hemorheology and patient anatomy on the hemodynamics in the inferior vena cava. *Ann. Biomed. Eng.* 44:3568–3582, 2016.
- <sup>3</sup>Aycock, K. I., R. L. Campbell, F. C. Lynch, K. B. Manning, and B. A. Craven. Computational predictions of the embolus-trapping performance of an IVC filter in patient-specific and idealized IVC geometries. *Biomech. Model. Mechanobiol.* 16:1957–1969, 2017.
- <sup>4</sup>Aycock, K. I., R. L. Campbell, K. B. Manning, S. P. Sastry, S. M. Shontz, F. C. Lynch, and B. A. Craven. A computational method for predicting inferior vena cava filter performance on a patient-specific basis. *J. Biomech. Eng.* 136:081003, 2014.
- <sup>5</sup>Bianchi, M., G. Marom, R. P. Ghosh, O. M. Rotman, P. Parikh, L. Gruberg, and D. Bluestein. Patient-specific simulation of transcatheter aortic valve replacement: impact of deployment options on paravalvular leakage. *Biomech. Model. Mechanobiol.* 18:435, 2018.
- <sup>6</sup>Chiastra, C., S. Morlacchi, D. Gallo, U. Morbiducci, R. Cardenes, I. Larrabide, and F. Migliavacca. Computational fluid dynamic simulations of image-based stented coronary bifurcation models. *J. R. Soc. Interface.* 10:20130193–20130193, 2013.
- <sup>7</sup>Craven, B. A., K. I. Aycock, L. H. Herbertson, and R. A. Malinauskas. A CFD-based Kriging surrogate modeling approach for predicting device-specific hemolysis power law coefficients in blood-contacting medical devices. *Biomech. Model. Mechanobiol.* 18:1005–1030, 2019.
- <sup>8</sup>Craven, B. A., M. M. Faghih, K. I. Aycock, and E. M. Kolahdouz. A Poisson equation method for prescribing fully developed non-Newtonian inlet conditions for computational fluid dynamics simulations in models of arbitrary cross-section. *Math. Comput. Simul.* 194:523–538, 2022.



- <sup>9</sup>Dixon, S. L., and C. A. Hall. Fluid Mechanics and Thermodynamics of Turbomachinery. Oxford: Butterworth-Heinemann, 2010.
- <sup>10</sup>Elkins, C. J., and M. T. Alley. Magnetic resonance velocimetry: applications of magnetic resonance imaging in the measurement of fluid motion. *Exp. Fluids*. 43:823–858, 2007.
- <sup>11</sup>Elkins, C., M. Markl, N. Pelc, and J. Eaton. 4D Magnetic resonance velocimetry for mean velocity measurements in complex turbulent flows. *Exp. Fluids*. 34:494–503, 2003.
- <sup>12</sup>FDA. Reporting of Computational Modeling Studies in Medical Device Submissions: Guidance for Industry and Food and Drug Administration Staff. <https://www.fda.gov/media/87586/download>, 2016.
- <sup>13</sup>Fraser, K. H., T. Zhang, M. Ertan Taskin, B. P. Griffith, and Z. J. Wu. A quantitative comparison of mechanical blood damage parameters in rotary ventricular assist devices: shear stress, exposure time and hemolysis index. *J. Biomech. Eng.* 134:081002, 2012.
- <sup>14</sup>Good, B. C., and K. B. Manning. Computational modeling of the Food and Drug Administration's benchmark centrifugal blood pump. *Artif. Organs*. 44:E263–E276, 2020.
- <sup>15</sup>Gundert, T. J., A. L. Marsden, W. Yang, and J. F. LaDisa. Optimization of cardiovascular stent design using computational fluid dynamics. *J. Biomech. Eng.* 134:011002, 2012.
- <sup>16</sup>Hariharan, P., K. I. Aycock, M. Buesen, S. W. Day, B. C. Good, L. H. Herbertson, U. Steinseifer, K. B. Manning, B. A. Craven, and R. A. Malinauskas. Inter-laboratory characterization of the velocity field in the FDA blood pump model using particle image velocimetry (PIV). *Cardiovasc. Eng. Technol.* 9:623–640, 2018.
- <sup>17</sup>Hariharan, P., M. Giarra, V. Reddy, S. W. Day, K. B. Manning, S. Deutsch, S. F. Stewart, M. R. Myers, M. R. Berman, G. W. Burgreen, E. G. Paterson, and R. A. Malinauskas. Multilaboratory particle image velocimetry analysis of the FDA benchmark nozzle model to support validation of computational fluid dynamics simulations. *J. Biomech. Eng.* 133:041002, 2011.
- <sup>18</sup>Herbertson, L. H., S. E. Olin, A. Daly, C. P. Noatch, W. A. Smith, M. V. Kameneva, and R. A. Malinauskas. Multilaboratory study of flow-induced hemolysis using the FDA benchmark nozzle model. *Artif. Organs*. 39:237–248, 2015.
- <sup>19</sup>ISO 14708-5:2020. Implants for Surgery—Active Implantable Medical Devices—Part 5: Circulatory Support Devices. Geneva, CH: International Organization for Standardization, 2020.
- <sup>20</sup>Kheradvar, A., E. M. Groves, A. Falahatpisheh, M. K. Mofrad, S. H. Alavi, R. Tranquillo, L. P. Dasi, C. A. Simmons, K. J. Grande-Allen, C. J. Goergen, F. Baaijens, S. H. Little, S. Canic, and B. Griffith. Emerging trends in heart valve engineering: part IV. Computational modeling and experimental studies. *Ann. Biomed. Eng.* 43:2314–2333, 2015.
- <sup>21</sup>Lee, J. H., A. D. Rygg, E. M. Kolahdouz, S. Rossi, S. M. Retta, N. Duraiswamy, L. N. Scotten, B. A. Craven, and B. E. Griffith. Fluid-structure interaction models of bioprosthetic heart valve dynamics in an experimental pulse duplicator. *Ann. Biomed. Eng.* 48:1475–1490, 2020.
- <sup>22</sup>Malinauskas, R. A., P. Hariharan, S. W. Day, L. H. Herbertson, M. Buesen, U. Steinseifer, K. I. Aycock, B. C. Good, S. Deutsch, K. B. Manning, and B. A. Craven. FDA benchmark medical device flow models for CFD validation. *ASAIO J.* 63:150–160, 2017.
- <sup>23</sup>Markl, M., F. P. Chan, M. T. Alley, K. L. Wedding, M. T. Draney, C. J. Elkins, D. W. Parker, R. Wicker, C. A. Taylor, R. J. Herfkens, and N. J. Pelc. Time-resolved three-dimensional phase-contrast MRI. *J. Magn. Resonance Imaging*. 17:499–506, 2003.
- <sup>24</sup>Marsden, A. L., Y. Bazilevs, C. C. Long, and M. Behr. Recent advances in computational methodology for simulation of mechanical circulatory assist devices. *Wiley Interdiscip. Rev. Syst. Biol. Med.* 6:169–188, 2014.
- <sup>25</sup>Morrison, T. M., M. L. Dreher, S. Nagaraja, L. M. Angelone, and W. Kainz. The role of computational modeling and simulation in the total product life cycle of peripheral vascular devices. *J. Med. Devices*. 11:024503, 2017.
- <sup>26</sup>Mueller, M., H. Schima, H. Engelhardt, A. Salat, D. Olsen, U. Losert, and E. Wolner. In vitro hematological testing of rotary blood pumps: remarks on standardization and data interpretation. *Artif. Organs*. 17:103–110, 1993.
- <sup>27</sup>Najjari, M. R., J. A. Hinke, K. V. Bulusu, and M. W. Plesniak. On the rheology of refractive-index-matched, non-Newtonian blood-analog fluids for PIV experiments. *Exp. Fluids*. 2016. <https://doi.org/10.1007/s00348-016-2185-x>.
- <sup>28</sup>Oberkampf, W. L., and C. J. Roy. Verification and Validation in Scientific Computing. Cambridge, UK: Cambridge University Press, 2010.
- <sup>29</sup>Pant, S., G. Limbert, N. P. Curzen, and N. W. Bressloff. Multiobjective design optimisation of coronary stents. *Biomaterials*. 32:7755–7773, 2011.
- <sup>30</sup>Pauli, L., J. Nam, M. Pasquali, and M. Behr. Transient stress-based and strain-based hemolysis estimation in a simplified blood pump. *Int. J. Numer. Methods Biomed. Eng.* 29:1148–1160, 2013.
- <sup>31</sup>Roache, P. J. Fundamentals of Verification and Validation. Socorro, New Mexico: Hermosa Publishers, 2009.
- <sup>32</sup>Song, X., A. L. Throckmorton, H. G. Wood, J. F. Antaki, and D. B. Olsen. Computational fluid dynamics prediction of blood damage in a centrifugal pump. *Artif. Organs*. 27:938–941, 2003.
- <sup>33</sup>Stewart, S. F., P. Hariharan, E. G. Paterson, G. W. Burgreen, V. Reddy, S. W. Day, M. Giarra, K. B. Manning, S. Deutsch, M. R. Berman, M. R. Myers, and R. A. Malinauskas. Results of FDA's first interlaboratory computational study of a nozzle with a sudden contraction and conical diffuser. *Cardiovasc. Eng. Technol.* 4:374–391, 2013.
- <sup>34</sup>Stewart, S. F., E. G. Paterson, G. W. Burgreen, P. Hariharan, M. Giarra, V. Reddy, S. W. Day, K. B. Manning, S. Deutsch, M. R. Berman, M. R. Myers, and R. A. Malinauskas. Assessment of CFD performance in simulations of an idealized medical device: results of FDA's first computational interlaboratory study. *Cardiovasc. Eng. Technol.* 3:139–160, 2012.
- <sup>35</sup>Stewart, S. F. C., R. A. Robinson, R. A. Nelson, and R. A. Malinauskas. Effects of thrombosed vena cava filters on blood flow: flow visualization and numerical modeling. *Ann. Biomed. Eng.* 36:1764–1781, 2008.
- <sup>36</sup>Walenga, R., C. Butler, B. Craven, P. Longest, R. Mohamed, B. Newman, B. Olsson, G. Hochhaus, B. Li, M. Luke, L. Zhao, A. Przekwas, and R. Lionberger. Mechanistic Modeling of Generic Orally Inhaled Drug Products (OIDPs): A Workshop Summary Report. *Clinical Pharmacology & Therapeutics: Pharmacometrics & Systems Pharmacology* (in press), 2022.

**Publisher's Note** Springer Nature remains neutral with regard to jurisdictional claims in published maps and institutional affiliations.